Chemical Science

ROYAL SOCIETY OF CHEMISTRY

EDGE ARTICLE

View Article Online
View Journal | View Issue

Check for updates

Cite this: *Chem. Sci.*, 2025, **16**, 22010

All publication charges for this article have been paid for by the Royal Society of Chemistry

Synergistic spin effects in medium-entropy Ni–Fe–Mn–Ce oxyhydroxides for seawater oxidation

Liyuan Xiao, Xue Bai, Zhenlu Wang and Jingqi Guan *

Received 10th July 2025
Accepted 16th October 2025

DOI: 10.1039/d5sc05118e

rsc.li/chemical-science

Efficient and durable oxygen evolution reaction (OER) electrocatalysis is essential for advancing sustainable seawater electrolysis. In this work, a high-performance Ni–Fe–Mn–Ce medium-entropy oxyhydroxide is constructed *via in situ* electrochemical reconstruction strategy for the OER. Guided by density functional theory (DFT), the effects of eight candidate fourth-metal elements (Al, Ce, Co, Cr, Cu, Sn, Zn, or Zr) on the electronic structure and reaction energetics of the NiFeMn(O)OH matrix are comprehensively investigated, revealing the unique advantages of Ce in optimizing intermediate adsorption energies and lowering the theoretical overpotential. The catalyst requires an overpotential of only 183 mV at 10 mA cm^{-2} in 1 M KOH, while maintaining a low overpotential of 224 mV in alkaline seawater, along with excellent resistance to Cl$^-$ corrosion. *Operando* spectroscopic characterizations reveal dynamic valence evolution and charge redistribution among Ni^{4+}, Fe^{3+}, and Ce^{3+}/Mn^{2+} species, which contribute to stabilizing intermediate adsorption and promoting electron transfer. Further electronic structure analysis demonstrates a favorable d-band center near the Fermi level and pronounces spin polarization in the medium-entropy system, which synergistically enhance OER kinetics. This work highlights the potential of entropy engineering combined with theoretical guidance in the development of advanced multi-metallic electrocatalysts for efficient seawater splitting.

Introduction

Electrochemical water splitting is considered one of the most promising technologies for large-scale hydrogen production, offering a sustainable pathway toward carbon neutrality.[1,2] Among the two half-reactions involved, the OER at the anode is particularly sluggish due to its complex four-electron transfer process and high kinetic barriers,[3–5] thereby limiting the overall efficiency of water electrolysis. Developing low-cost, high-performance, and durable OER electrocatalysts is thus crucial for enabling practical hydrogen production. Transition-metal (oxy)hydroxides, especially NiFe-based materials, have emerged as state-of-the-art non-precious OER catalysts in alkaline environments due to their earth abundance, favorable redox chemistry, and tunable electronic structures.[6–8] Recent studies have further demonstrated that the electrochemically reconstructed (oxy)hydroxides are the true active species during OER. For instance, surface-reconstructed (CoNiFe)OOH derived from its parent alloy has been reported as the real catalytically active phase.[9] Similarly, oxyhydroxide products can also be generated from the corresponding hydroxides under anodic polarization.[10] These findings highlight the universal tendency of transition-metal precursors to transform into (oxy)hydroxides as the real active phases during OER. However, their catalytic performance is still restricted by limited intrinsic activity, sluggish electron transfer, and suboptimal adsorption of reaction intermediates.[11,12] To overcome these limitations, multi-metallic engineering strategies have attracted increasing attention, wherein the incorporation of a third transition metal such as Mn has shown promise in modulating the local coordination environment, inducing oxygen vacancies, and enhancing charge transport.[13,14] Zhang *et al.* demonstrated that the incorporation of Fe and Co into Ni-based catalysts can regulate the structural transformation from hydroxide to oxide phases, forming ternary metal active sites and significantly reducing the OER overpotential to 146 mV. In particular, the introduction of Co tunes the electron distribution and d-orbital occupancy, optimizes the adsorption energies of reaction intermediates, lowers the energy barriers, and enhances the magnetic moment, thereby further improving the catalytic activity.[15]

More recently, the concept of medium-entropy catalysts (MECs), involving three to four principal metallic elements, has emerged as a powerful strategy to enhance catalytic activity through synergistic electronic effects and structural stability.[16,17] Unlike high-entropy alloys that may suffer from over-randomization and potential activity dilution,[18] MECs offer a balance between compositional complexity and performance optimization.[19] The presence of multiple active centers, coupled with enhanced charge redistribution and flexible orbital occupancy, enables favorable adsorption energies for key OER

Institute of Physical Chemistry, College of Chemistry, Jilin University, Changchun 130021, PR China. E-mail: guanjq@jlu.edu.cn

intermediates and improved reaction kinetics. Wu *et al.* demonstrated that the medium-entropy metal sulfide $Fe_{1.2}(CoNi)_{1.8}S_6$ exhibited excellent activity and stability for OER.[17] Sulfidation increased the valence state of the active sites, thereby lowering the reaction energy barrier and accelerating reaction kinetics. DFT calculations revealed that the medium-entropy configuration effectively modulates the electronic structure, reduces charge transfer resistance, and enhances chemical bonding strength, resulting in improved catalytic efficiency. Huang *et al.* prepared porous CoNiFe alloys[20] *via* phosphate decoration and $CoNiFeCu_{0.1}$ alloys[21] *via* a solution combustion method, effectively tuning the metal composition and surface structure, which enhanced electron transport and the distribution of active sites, thereby exhibiting excellent catalytic activity and long-term stability for the OER. Moreover, the configurational entropy contributes to structural robustness, particularly under harsh electrochemical conditions.[22]

At the same time, alkaline seawater electrolysis is gaining attention as a viable route to sustainable hydrogen production by directly utilizing abundant natural seawater.[23] However, the presence of aggressive ions, such as Cl^-, Mg^{2+}, and Ca^{2+}, imposes significant challenges, including electrode corrosion, competitive chlorine evolution reactions (ClER), and precipitation-induced passivation.[24–26] These issues demand electrocatalysts with OER activity, exceptional selectivity and durability in seawater electrolysis. The combination of medium-entropy design and robust oxyhydroxide frameworks presents a compelling route to tackle these challenges simultaneously.

In this study, a novel Ni–Fe–Mn–Ce medium-entropy oxyhydroxide catalyst was developed for efficient and stable OER in both alkaline and alkaline seawater conditions. Building on previous work that established the Ni–Fe–Mn ternary system as a promising OER catalyst,[27] DFT was employed to screen eight potential fourth metal elements. Among them, Ce was identified as the optimal dopant due to its ability to tune the electronic structure, lower intermediate adsorption energies, and improve the reaction pathway. Guided by these insights, $NiFeMnCe_{0.8}(O)OH/NF$ was successfully synthesized *via* an *in situ* electrochemical reconstruction method on nickel foam. Electrochemical tests in 1 M KOH and alkaline seawater demonstrated excellent OER activity and long-term stability. Combined *operando* fourier transform infrared spectroscopy (FTIR), *operando* Raman, and XPS analyses revealed the valence evolution and synergistic interactions among the metal components during OER. Further theoretical calculations of density of states (DOS), d-band center, and reaction free energy diagrams confirmed the essential role of Ce in optimizing the electronic structure and lowering reaction energy barriers.

Results and discussion

To evaluate the theoretical OER catalytic performance of the Ni–Fe–Mn-M (M = Al, Ce, Co, Cr, Cu, Sn, Zn, and Zr) oxyhydroxides, we computed the ΔG values of key intermediates using DFT. As illustrated in Fig. 1a, the OER process follows the conventional adsorbate evolution mechanism (AEM), comprising four sequential steps:[28] (1) OH^- adsorption to form *OH; (2) deprotonation of *OH to generate *O; (3) coupling of *O with OH^- to form *OOH; and (4) desorption of *OOH to release O_2 and regenerate the active site. The computational results indicate that the *OH → *O and *O → *OOH steps are potential rate-determining steps. Notably, the AEM pathway exhibits lower activation energy barriers for the reaction intermediates and transition states compared to alternative mechanisms, demonstrating its thermodynamic feasibility. Consistent with previous mechanistic analyses of NiFe-based catalysts under alkaline conditions, the AEM is identified as the more plausible descriptor for the OER behavior in this system.[29,30] Building upon the conventional two-dimensional volcano plot framework, this study introduces ΔG_{*OOH} as a third dimension to construct a three-dimensional reaction energy barrier model (Fig. 1b). The *x*-axis ($\Delta G_{*O} - \Delta G_{*OH}$) quantifies the thermodynamic driving force for the *OH → *O transition, reflecting the kinetic barriers associated with the second OER step. The *y*-axis represents the theoretical overpotential (η), serving as a universal descriptor for the minimum electrochemical potential required to drive the overall reaction. The *z*-axis (ΔG_{*OOH}) characterizes the adsorption strength of the *OOH intermediate, critically influencing the thermodynamic feasibility of the third OER step (*O → *OOH). This three-dimensional energy landscape enables a more comprehensive analysis of the synergistic interplay among intermediate adsorption energies, thereby transcending the limitations of traditional volcano plots that focus exclusively on single-step energy barriers. Conventionally, an optimal $\Delta G_{*O} - \Delta G_{*OH}$ value near 1.6 eV is desired to balance the adsorption strengths of *OH and *O intermediates.[31] Remarkably, the NiFeMnCe(O)OH system exhibits the lowest theoretical overpotential despite deviating from this optimal range on the *x*-axis. This apparent discrepancy suggests superior synergistic tuning of key intermediate adsorption energies across the entire reaction pathway. Detailed analysis reveals that NiFeMnCe(O)OH achieves this performance through moderate *OOH adsorption strength along the ΔG_{*OOH} dimension, which effectively compensates for the elevated energy barrier of the *OH → *O step and enables holistic optimization of the overall reaction energy profile. Thus, the three-dimensional energy model thus uncovers the multifactorial synergistic nature governing OER activity, demonstrating how NiFeMnCe(O)OH achieves minimal theoretical overpotential through coordinated optimization of adsorption energies among critical intermediates.

In order to verify the accuracy of theoretical simulations, we fabricated a series of NiFeMnM(O)OH/NF electrocatalysts by a dynamic anodic reconstruction strategy (Fig. 2a). Taking NiFeMnCe(O)OH/NF as an example, hydrothermally synthesized NiFeMnCe-TPA/NF (TPA = terephthalic acid) was used as the precursor, and constant potential polarization was applied in 1.0 M KOH electrolyte to induce *in situ* structural reconstruction to form NiFeMnCe(O)OH/NF. This process involves ligand dissociation and formation of metal oxyhydroxide species, enabling the transformation from precursor to active phase. The surface morphology and microstructure of the catalyst before and after reconstruction were systematically characterized by scanning electron microscopy (SEM) and

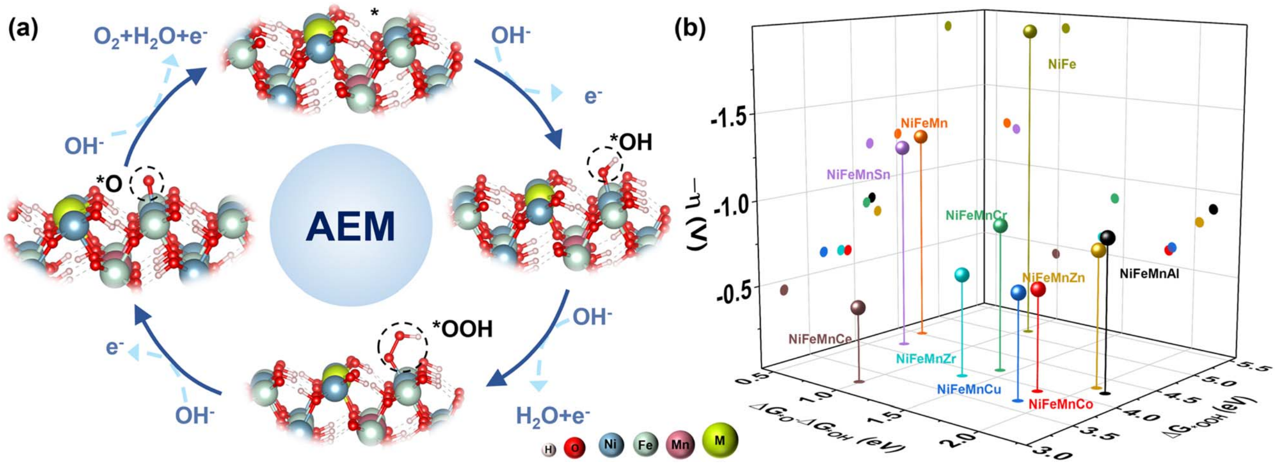

Fig. 1 (a) AEM on NiFeMnM(oxy)hydroxide. (b) Three-dimensional reaction energy barrier model.

transmission electron microscopy (TEM). SEM images reveal that the NiFeMnCe-TPA/NF precursor exhibited petal-like hierarchical nanosheet architecture with typical layered topological feature (Fig. 2b and S1). TEM analysis further confirms the presence of sharply defined ultrathin nanosheet stacks at the edges, highlighting the two-dimensional layered nature (Fig. 2c). High-resolution TEM (HRTEM) images (Fig. 2d and f) reveal a multi-phase crystalline precursor, as evidenced by the presence of multiple lattice fringe sets. Among these, the two most prominent and measurable spaces of 0.21 nm and 0.23 nm are indexed to specific phases. The 0.21 nm spacing is assigned to the (003) plane of the Ni-TPA phase, as determined by simulation using its crystal structure (CIF file) in VESTA software. The 0.23 nm spacing corresponds to the (121) plane of a NiO·NiOOH-like phase, consistent with the standard powder diffraction file (PDF#40-1179). Energy-dispersive X-ray spectroscopy (EDX) mapping reveals the uniform distribution of Ni, Fe, Mn, and Ce elements, indicating successful incorporation of these metal components (Fig. S2). After electrochemical reconstruction, the SEM images display a transformation into a three-dimensional porous layered structure with interlaced nanosheets (Fig. 2g). TEM observations indicate significant modulation of interlayer spacing, along with increased local lattice distortion and defect density (Fig. 2h). HRTEM analysis reveals the disappearance of long-range crystalline order in the reconstructed regions (Fig. 2i), suggesting a phase transition from crystalline to amorphous state during the activation process.[32] This structural evolution is expected to expose more active sites and enhance mass transport pathways, thereby improving catalytic performance. Post-reconstruction EDX mapping of the NiFeMnCe(O)OH/NF catalyst continues to show a homogeneous distribution of Ni, Fe, Mn, and Ce, confirming the compositional uniformity and structural stability (Fig. 2j).

X-ray diffraction (XRD) analysis reveals pronounced structural evolution of the catalyst with varying reconstruction durations (Fig. 2k). Initially, the XRD patterns display distinct diffraction peaks corresponding to Ni-TPA (PDF#35-1676), Fe-TPA (PDF#33-1724), and NiO·NiOOH (PDF#40-1179). After 5 minutes of reconstruction, the characteristic peaks of Ni-TPA and Fe-TPA were significantly reduced or completely vanished, while the intensity of NiO·NiOOH peaks increased, accompanied by the emergence of new peaks assigned to FeOOH (PDF#26-0792). With reconstruction extended to 15 minutes, all diffraction signals further weakened, and by 30 minutes, all crystalline peaks completely disappeared, indicating the formation of an amorphous phase.[33] These findings correlate consistently with HRTEM observations.

Under constant voltage, the current density of NiFeMnCe-TPA/NF initially rises, then gradually falls, and finally keeps stable (Fig. 2l). *Operando* Raman spectroscopy was used to study this dynamic change. The initial Raman spectrum shows TPA ligand vibrations at specific wavenumbers (in-plane: 1611, 1438, and 1132 cm^{-1}; out-of-plane: 854, 813, and 630 cm^{-1}),[34,35] confirming successful synthesis of NiFeMnCe-TPA/NF (Fig. S3). After the immersion in KOH solution, the TPA ligand signals disappear, indicating ligand degradation and exposure of metal active sites. During dynamic structural reconstruction, two novel Raman peaks emerge at 479 cm^{-1} and 556 cm^{-1} during the initial 5-minute reconstruction phase (Fig. 2m). These peaks are assigned to the E_g bending vibration of Ni^{3+}–O in γ-NiOOH[36] and the A_{1g} stretching vibration of Fe^{3+}–O in γ-FeOOH,[37] respectively, directly confirming the *in situ* formation of Ni–Fe oxyhydroxide active phases. The observation of peak broadening further suggests a catalytic morphology characterized by short-range atomic order yet long-range disorder, indicative of amorphous structure development post-reconstruction.[38] Upon extending the reconstruction duration to 0.5 hours, a distinct F_{2g} vibrational mode appears in the 452–455 cm^{-1} range, corresponding to Ce^{4+}–O bonding (Fig. 2m). Notably, this peak exhibits a red shift (460–465 cm^{-1} in pure CeO_2), which can be attributed to Ni^{2+}/Mn^{3+} doping-induced Ce–O bond length relaxation and lattice distortion effects.[39,40] Continuous enhancement of Ce^{4+}–O F_{2g} peak intensity with prolonged reconstruction times suggests a phase transformation pathway: metastable CeOOH intermediates likely undergo dehydroxylation to form thermodynamically stable CeO_2 phases.

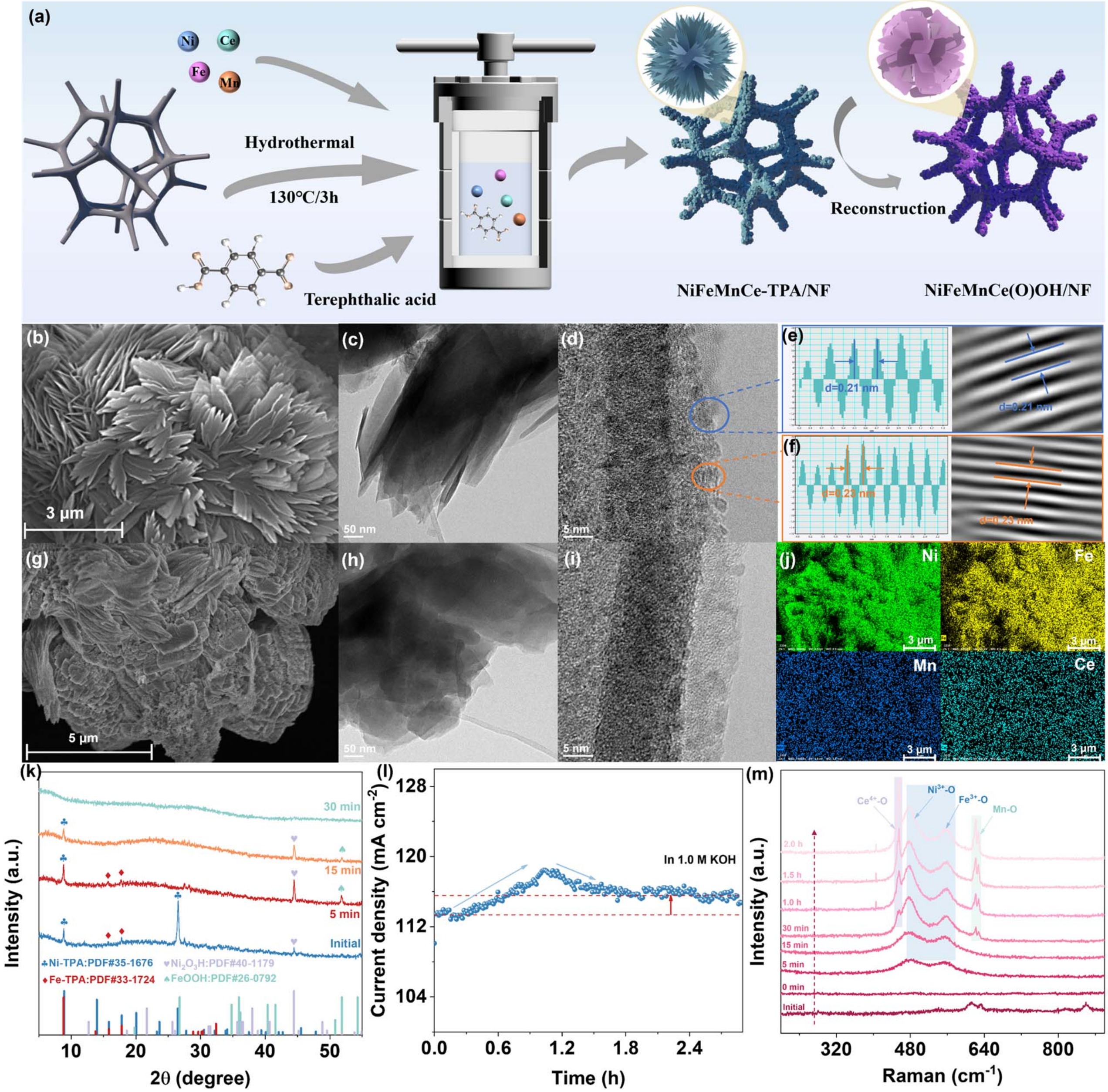

Fig. 2 (a) Schematic diagram of the preparation of NiFeMnCe(O)OH/NF. (b) SEM, (c) TEM, and (d) HRTEM characterization of NiFeMnCe-TPA/NF. (e and f) FFT images of the matrix. (g) SEM, (h) TEM, (i) HRTEM, and (j) EDX characterization of NiFeMnCe(O)OH/NF. (k) *Operando* XRD patterns. (l) Anodic reconstruction curve. (m) *Operando* Raman spectra.

Concurrently, the emergence of a strong Mn–O A_{1g} vibrational peak at 622–627 cm^{-1} provides spectroscopic evidence for the formation of NiFeMn–OOH ternary oxyhydroxide active species (Fig. 2m).[41,42]

Kinetic analysis reveals that the electrochemical reconstruction proceeds through a three-stage dynamic evolution. Initially, the strongly alkaline electrolyte removes TPA ligands, exposing Ni/Fe metal centers that are progressively oxidized to form active NiOOH and FeOOH phases, leading to an increase in current density. As the process continues, some high-energy intermediates may restructure or convert into more stable but less active oxides. At the same time, surface metals may be over-oxidized to high-valence states (*e.g.*, Ni^{4+}, Mn^{4+}), which have unfavorable electronic structures for intermediate adsorption, thus hindering OER performance. Eventually, the surface forms a stable, multi-phase, medium-entropy oxyhydroxide layer with uniform electronic properties and stable active sites, ensuring long-term catalytic activity and steady current output.

The excellent OER performance and the mechanism on the NiFeMnCe(O)OH/NF catalyst are revealed by systematic electrochemical analysis. Linear sweep voltammetry (LSV) curves indicate that in 1 M KOH, the catalyst exhibits a low overpotential (η_{10}) of only 183 mV at 10 mA cm^{-2}, which is significantly lower than those of NiFeMnM(O)OH/NF catalysts

(M = Al: 222 mV, Co: 198 mV, Cr: 201 mV, Cu: 199 mV, Sn: 247 mV, Zn: 202 mV, Zr: 213 mV) (Fig. 3a). These results are consistent with theoretical calculations, confirming outstanding OER activity of the NiFeMnCe(O)OH/NF. Ce features a unique 4f electronic structure, enabling it to serve as an additional electron donor or acceptor. However, excessive Ce can disrupt surface electron distribution, hindering water adsorption and activation. To optimize the OER performance, the effect of Ce doping was investigated. As illustrated in Fig. 3b, the $NiFeMnCe_{0.8}(O)OH/NF$ catalyst, with a stoichiometric ratio of Ni : Fe : Mn : Ce = 1 : 1 : 1 : 0.8, demonstrates the optimal OER activity, achieving a low η_{10} of 181 mV. This performance is comparable to that of state-of-the-art OER catalysts reported in recent studies (Fig. 3c and Table S1)[18,20,21,43–47] and surpasses that of the benchmark IrO_2 catalyst (η_{10} = 245 mV). Original LSV curves (without *iR* compensation) for all samples are provided in (Fig. S4a–c) to allow Tafel slope calculations. In addition, a comparison of the overpotentials at 10 mA cm^{-2} for *iR*-compensated and uncompensated data is included in Table S2. Remarkably, it delivers up to 500 mA cm^{-2} at only 265 mV. Comparison with single-doped systems highlights the key role of Mn/Ce synergy in enhancing OER kinetics. Relative to NiFe(O)OH/NF, which shows an overpotential of 208 mV at 10 mA cm^{-2} and a Tafel slope of 46.4 mV dec^{-1}, individual incorporation of Ce or Mn reduces the overpotential to 210 or 191 mV, with corresponding Tafel slopes of 37.1 or 33.6 mV dec^{-1} (Fig. 3d). These improvements suggest that each dopant independently enhances OER kinetics by modulating the electronic environment. Remarkably, Mn and Ce codoping in $NiFeMnCe_{0.8}(O)OH/NF$ leads to a pronounced synergistic effect, achieving a substantially lower overpotential of 181 mV and a Tafel slope of 29.4 mV dec^{-1}. This enhancement is attributed to the moderate configurational entropy introduced by dual doping, which promotes balanced adsorption–desorption kinetics and significantly improves overall catalytic activity. Electrochemical impedance spectroscopy (EIS) was used to monitor the reconstruction of the $NiFeMnCe_{0.8}(O)OH/NF$ pre-catalyst. As shown in Fig. S4d, the Nyquist plots gradually shrink with activation time, indicating a continuous decrease in charge transfer resistance (R_{ct}). The spectra at 90 and 120 min are almost identical, showing that the transformation into a highly conductive active phase is essentially complete after 90 min. Among the fully reconstructed catalysts, $NiFeMnCe_{0.8}(O)OH/NF$ has the smallest semicircle, confirming the lowest R_{ct} (Fig. 3e). This improvement is mainly due to the combined effect of Mn and Ce doping: Mn increases bulk

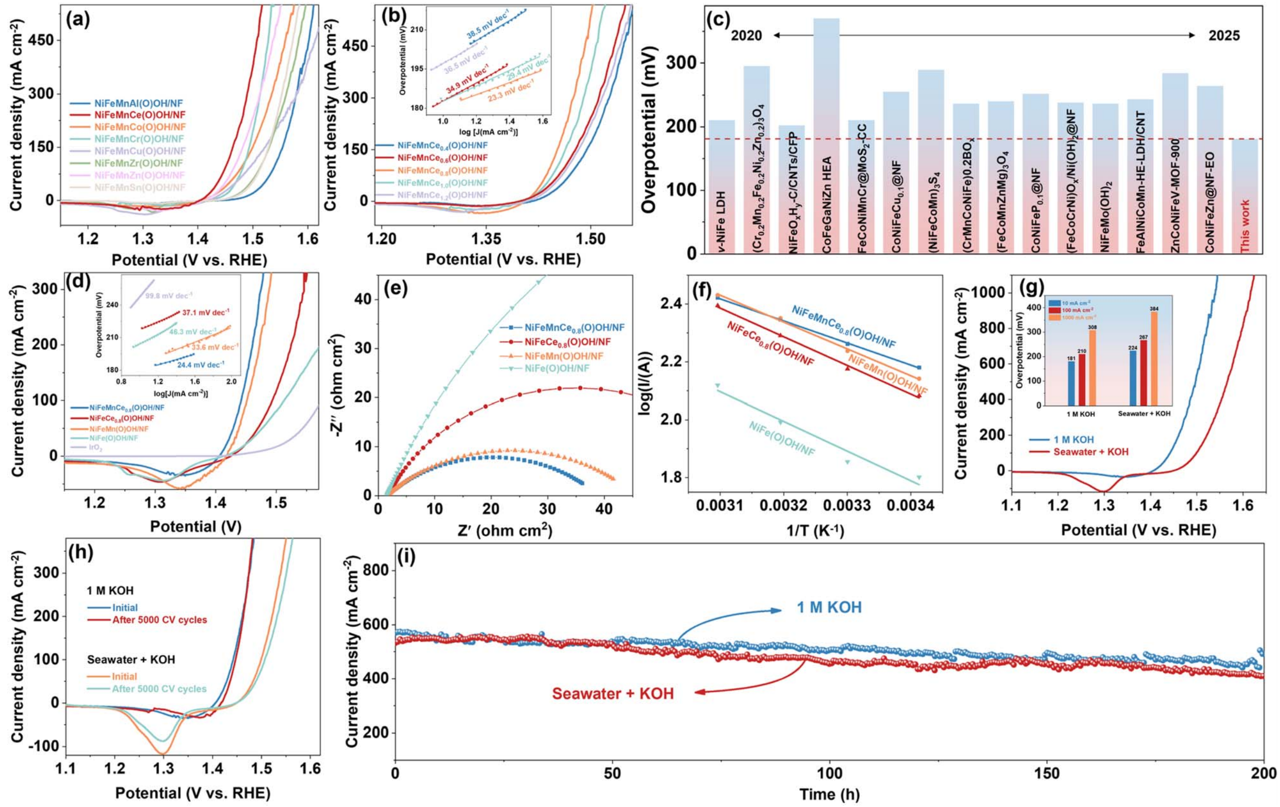

Fig. 3 LSV curves of (a) NiFeMnM(O)OH/NF and (b) $NiFeMnCe_x(O)OH/NF$ with 90% *iR*-compensation. (c) Comparison of overpotential at 10 mA cm^{-2} in 1 M KOH. (d) LSV curves of NiFe(O)OH/NF, NiFeMn(O)OH/NF, $NiFeCe_{0.8}(O)OH/NF$ and $NiFeMnCe_{0.8}(O)OH/NF$ with 90% *iR*-compensation. The inset shows the corresponding Tafel slope. (e) Nyquist plots. (f) Arrhenius plots. (g) LSV curves in 1 M KOH and alkaline seawater with 90% *iR*-compensated. The illustration shows the comparison of overpotential at 10, 100, and 1000 mA cm^{-2}. (h) The comparison chart of LSV before and after the CV cycles with 90% *iR*-compensation. (i) Chronoamperometric response of $NiFeMnCe_{0.8}(O)OH/NF$ in 1 M KOH and alkaline seawater.

conductivity by providing extra charge carriers, while Ce with its 4f orbitals tunes the surface electronic structure to facilitate charge transfer. As shown in Fig. S5, $NiFeMnCe_{0.8}(O)OH/NF$ exhibits an electrochemical active surface area (ECSA) of 154 cm^2, markedly higher than NiFe(O)OH/NF (94 cm^2), NiFeMn(O)OH/NF (126 cm^2), and $NiFeCe_{0.8}(O)OH/NF$ (106 cm^2). These results demonstrate that Mn–Ce co-doping synergistically enhances the exposure of active sites. Ce-incorporated catalysts ($NiFeCe_{0.8}(O)OH/NF$, $NiFeMnCe_{0.8}(O)OH/NF$) show a negative shift in cyclic voltammetry (CV) curves compared to Ce-free ones (NiFe(O)OH/NF, NiFeMn(O)OH/NF), reflecting Ce^{3+}/Ce^{4+}-mediated modulation of the electrode–electrolyte interface. This shift does not affect ECSA values derived from scan-rate-dependent current differences. LSV measurements were conducted between 298 and 348 K to generate Arrhenius plots of the natural logarithm of current density *versus* inverse temperature (Fig. 3f and S6), allowing accurate determination of the activation energy (E_a). $NiFeMnCe_{0.8}(O)OH/NF$ displays a notably lower E_a of 14.6 kJ mol^{-1} than NiFe(O)OH/NF (19.6 kJ mol^{-1}), NiFeMn(O)OH/NF (17.8 kJ mol^{-1}), and $NiFeCe_{0.8}(O)OH/NF$ (19.0 kJ mol^{-1}). The quaternary metal synergy enables fine tuning of the OER pathway *via* multidimensional electronic modulation. Importantly, the multivalent nature of Ce and Mn facilitates cooperative catalysis by effectively balancing intermediate adsorption and desorption energies. Moreover, the catalyst exhibits a notable positive shift in the LSV curve in 0.1 M KOH compared to 1 M KOH (Fig. S7), indicating enhanced OER activity with increasing OH^- concentration and pH dependence. This behaviour is consistent with the kinetic characteristics of the AEM, supporting a reaction pathway in which OH^- acts as a direct reactant.[48–50]

Building on the superior OER activity of $NiFeMnCe_{0.8}(O)OH/NF$ in alkaline media, its performance was further assessed in a practical alkaline seawater environment by dissolving 1 M KOH in natural seawater. The catalyst requires an overpotential of only 224 mV at 10 mA cm^{-2} (Fig. 3g and S8), which is merely 43 mV higher than that under analogous freshwater conditions. At 100 mA cm^{-2}, the overpotential remains as low as 265 mV, demonstrating competitive performance among electrocatalysts reported to date for alkaline seawater electrolysis (Fig. S9 and Table S3). Remarkably, at an industrial current density of 1 A cm^{-2}, the overpotential remained low at 384 mV (Fig. 3g), substantially below the onset potential of the competing chlorine evolution reaction (480 mV),[51,52] with a margin of 96 mV that effectively mitigates catalyst corrosion from Cl^--induced side reactions. The catalytic durability of $NiFeMnCe_{0.8}(O)OH/NF$ was verified *via* cyclic voltammetry (CV) cycling and chronoamperometric measurements in both 1 M KOH and alkaline seawater electrolytes. As shown in Fig. 3h, after 5000 CV cycles in 1 M KOH, polarization curves overlapped closely with minimal overpotential increase ($\Delta\eta_{100} = 3.9$ mV), indicating stable active sites. In alkaline seawater, slight performance decline was observed ($\Delta\eta_{100} = 8.4$ mV), attributed to Cl^- blocking active sites and catalyst poisoning by insoluble precipitates. Chronoamperometric measurements (Fig. 3i) demonstrate sustained operation at industrial current densities, with current density decreasing modestly from 570 to 511 mA cm^{-2} after 200 h in 1 M KOH. In alkaline seawater, the current density of the catalyst decreased from 532 mA cm^{-2} to 424 mA cm^{-2}, but the OER stability of this catalyst remained competitive among the reported catalysts.[52–56]

To investigate surface structural changes, *operando* FTIR spectroscopy was conducted on $NiFeMnCe_{0.8}(O)OH/NF$ under different OER potentials. The C=O stretching band at 1680 cm^{-1} weakens with increasing potential,[57] indicating the removal or transformation of surface carbonyl groups during catalysis. At higher potentials, a broad band appears around 3300 cm^{-1}, assigned to the O–H stretching of adsorbed water ($*H_2O$) or hydrated hydroxyls ($*OH_2$), which gradually shifts toward the region characteristic of adsorbed hydroxyls (*OH) (Fig. 4a).[58] This shift suggests that OH^- ions penetrate the surface, modulating the interfacial structure and promoting the formation of active sites. *Operando* Raman spectroscopy of $NiFeMnCe_{0.8}(O)OH/NF$ under alkaline seawater conditions shows clear structural evolution with increasing applied potential. The characteristic Ni–O and Fe–O bands at around 470 cm^{-1} and 560 cm^{-1} gradually intensify, indicating the electrochemical oxidation of Ni and Fe sites into active NiOOH and FeOOH phases (Fig. 4b).[59,60] These results directly confirm the *in situ* formation of NiOOH and FeOOH phases during reconstruction, consistent with previous observations that (oxy)hydroxides are the true active species for the OER.[9,10] Meanwhile, a broad band appears in the 900–1100 cm^{-1} region, corresponding to *OOH and other key OER intermediates, suggesting that the OER proceeds efficiently in alkaline seawater.[61]

Quantifying the chlorine evolution reaction (CER) in alkaline media *via* gas-phase analysis is difficult because Cl_2 rapidly hydrolyzes to form OCl^-, leading to significant underestimation of CER faradaic efficiency. The gaseous Cl_2 detected only represents a small fraction of the total chlorine produced, dependent on mass transfer. To better assess chloride-ion reactions, this study combines ion chromatography (IC) with post-reaction electrode characterization (SEM-EDX). IC measurements (Fig. 4c) reveal that the Cl^- concentration in the electrolyte decreases during alkaline seawater electrolysis for all catalyst systems, suggesting the occurrence of Cl^--consuming processes. However, the $NiFeMnCe_{0.8}(O)OH/NF$ catalyst exhibits the smallest decrease in Cl^- concentration, markedly outperforming the other catalysts. This minimal Cl^- consumption, coupled with the high OER activity, implies that this catalyst is the most effective in mitigating undesirable reactions involving chloride ions. This result suggests that the synergistic effect among multiple metal components effectively regulates the surface electronic structure, leading to the observed reduction in Cl^- consumption. Further SEM-EDX analysis of the post-reaction $NiFeMnCe_{0.8}(O)OH/NF$ catalyst reveals a uniform distribution of Cl on the surface (Fig. S10a and b). Together with the minimal change in Cl^- concentration in the electrolyte, this strongly suggests that the detected Cl species primarily result from limited adsorption of Cl^- at active sites, rather than from continuous CER. These adsorbed Cl species likely form a protective interfacial layer that passivates the surface. We propose that this passivation layer effectively

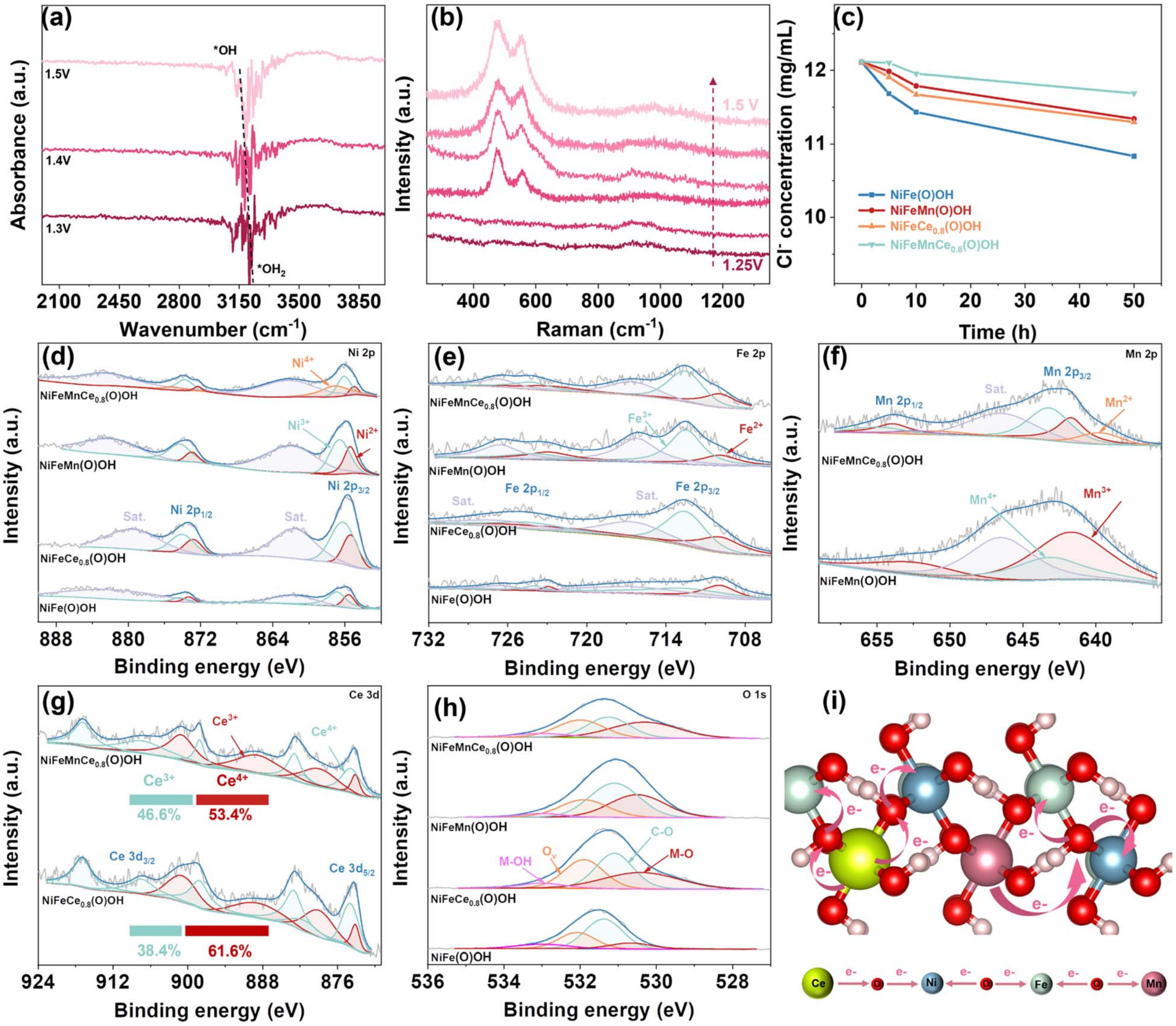

Fig. 4 (a) *Operando* FTIR spectra of $NiFeMnCe_{0.8}(O)OH$. (b) *Operando* Raman of $NiFeMnCe_{0.8}(O)OH$. (c) Cl^- concentration after reaction determined by IC. XPS spectra of (d) Ni 2p, (e) Fe 2p, (f) Mn 2p, (g) Ce 3d and (h) O 1s. (i) Schematic diagram of charge transfer.

limits further extensive Cl^- oxidation, which is consistent with the observed stability of Cl^- concentration in the bulk electrolyte. Overall, the combination of minimal Cl^- consumption and surface Cl adsorption points to a surface chloride-passivation mechanism on $NiFeMnCe_{0.8}(O)OH$/NF. This mechanism appears to be highly effective in minimizing chloride-related side reactions, thereby promoting a stable OER process. Despite the minimal consumption of Cl^-, the current density gradually decreased by approximately 20% during 200 hours of continuous operation. To investigate the cause of this decay, this study focused on the deposition of insoluble inorganic salts during seawater electrolysis. SEM image of the catalyst after the stability test (Fig. S10a) reveals that its surface is covered with blocky crystalline deposits, and EDX analysis further confirms that these deposits are rich in Ca and Mg (Fig. S10c and d), indicating the formation of inorganic scale. The significant decrease in Ca^{2+} and Mg^{2+} concentrations in the electrolyte was confirmed by inductively coupled plasma optical emission spectroscopy (ICP-OES) (Fig. S11). These results suggest that the gradual decrease in current density is mainly due to the physical coverage of active sites and pore blockage by these insulating deposits, which hinder mass transport and reduce the electrochemically active surface area. In contrast, the surface chlorine species form a passivating layer that does not block pores or cover active sites. Thereby, the root cause of the current decay is conclusively attributed to the deposition of inorganic salts under high interfacial pH conditions during the OER.

To gain deeper insight into the evolution of the electronic structure in NiFe(O)OH, NiFeMn(O)OH, $NiFeCe_{0.8}(O)OH$ and $NiFeMnCe_{0.8}(O)OH$ and its impact on OER performance, XPS was conducted. Fig. S12 displays the presence of Ni, Fe, Mn, Ce and O elements in $NiFeMnCe_{0.8}(O)OH$ electrocatalyst. As shown in Fig. 4d, the Ni $2p_{3/2}$ spectrum of NiFe(O)OH can be deconvoluted into two main peaks corresponding to Ni^{2+} (855.4 eV) and Ni^{3+} (856.7 eV),[62] along with a prominent satellite peak, indicating partial oxidation of Ni and a certain degree of electron localization. The introduction of either Mn or Ce individually increases the proportion of Ni^{3+}, suggesting an elevated average oxidation state of Ni. Notably, in NiFeMnCe$_{0.8}$(O)OH, the main peak shifts further to 856.3 eV, accompanied by the emergence of Ni^{4+} shoulder and significant reduction in satellite intensity, indicating that Mn–Ce co-doping effectively stabilizes Ni^{4+}, enhances electronic delocalization, and thus improves both electron conductivity and intermediate regulation. The Fe 2p spectrum reveals the coexistence of Fe^{2+} and Fe^{3+} species (Fig. 4e).[63] Compared to the other samples, NiFeMnCe$_{0.8}$(O)OH shows a significantly increased Fe^{3+}/Fe^{2+} ratio, a slight blue shift in the main peak, a more symmetrical Fe $2p_{1/2}$ peak shape, and reduced satellite intensity. These features suggest a higher average oxidation state of Fe, a more stable valence distribution, and enhanced Fe–O covalency, leading to a more optimized electronic structure that benefits OER activity. The Mn $2p_{3/2}$ spectrum indicates that Mn primarily exists as Mn^{3+} (641.7 eV) and Mn^{4+} (643.2 eV) in NiFeMn(O)OH (Fig. 4f),[64] demonstrating high oxidation state stability. In NiFeMnCe$_{0.8}$(O)OH, an additional shoulder peak appears at lower binding energy (639.7 eV), corresponding to Mn^{2+}, indicating a bipolar distribution of Mn valence states from low to high.[65,66] This distribution facilitates charge state regulation at Mn sites and improves the dynamic modulation of oxygen intermediates, thereby enhancing the synergistic catalytic performance of the system. The Ce 3d spectrum provides further insight into the valence state evolution of Ce (Fig. 4g).[67,68] In NiFeMnCe$_{0.8}$(O)OH, an increase in the Ce^{3+} peak area alongside a decrease in Ce^{4+} peaks indicates partial reduction of Ce^{4+} induced by Mn doping. This reduction can be attributed to: (1) charge compensation driven by Mn^{4+}, and (2) Mn-induced lattice distortion and oxygen vacancy formation, which help stabilize Ce^{3+} species. The higher Ce^{3+} content enhances charge carrier mobility, improves adsorption of key OER intermediates, and contributes to a more favorable electronic structure for OER. Deconvolution of the O 1s spectra reveals four main components in all samples: M–O (530.5 eV), M–OH (533.0 eV), oxygen vacancies (531.9 eV), and C–O species (531.1 eV) (Fig. 4h).[68] Compared to NiFe(O)OH, both NiFeCe$_{0.8}$(O)OH and NiFeMn(O)OH show a shift of the O 1s main peak to lower binding energies, indicating increased electron density and a more reduced local environment due to Ce or Mn doping. Mn, in particular, has a stronger effect on promoting oxygen vacancy formation. In NiFeMnCe$_{0.8}$(O)OH, the O 1s main peak shows a slight increase in binding energy compared to singly doped samples but remains lower than that of the undoped material, indicating a synergistic effect between Mn and Ce. As shown in Fig. 4i, high-valent Ni^{4+} and Fe^{3+} withdraw electrons from nearby oxygen atoms ($O \rightarrow Ni^{4+}/Fe^{3+}$), increasing their oxidation states and reactivity. In contrast, Mn^{2+} and Ce^{3+} donate electrons to oxygen ($Mn^{2+}/Ce^{3+} \rightarrow O$), helping to balance charge and stabilize the structure. Additionally, Mn^{4+} promotes the reduction of Ce^{4+} to Ce^{3+}, with the released electrons transferred through oxygen bridges to metal sites, enabling efficient charge redistribution.

To elucidate the role of spin polarization in enhancing OER kinetics and the superior performance of NiFeMnCe$_{0.8}$(O)OH, we combined external magnetic field experiments with spin-polarized DFT calculations. Under a ±0.3 T magnetic field, NiFeMnCe$_{0.8}$(O)OH exhibited a significantly reduced overpotential of 27 mV at 100 mA cm^{-2} alongside a distinct decrease in Tafel slope from 45.2 to 33.4 and 31.7 mV dec^{-1}, as shown in Fig. 5a. These results clearly demonstrate a pronounced magneto-spin effect. This enhancement stems from magnetic alignment of spins *via* the Zeeman effect, which promotes spin-selective charge transfer and reduces spin-related barriers during O_2 evolution. DFT results reveal consistently high spin polarization ratios (20–22%) among all investigated catalysts (Fig. 5b), demonstrating that spin polarization is an inherent property of these (oxy)hydroxide materials. However, only NiFeMnCe$_{0.8}$(O)OH shows significant catalytic improvement. Comparative energy barrier calculations confirm that spin polarization markedly lowers the energy of the potential-determining step (O* → OOH*), thermodynamically validating its key role in enhancing OER kinetics (Fig. 5c).

The results of total density of states (TDOS) show that the NiFeMnCe$_{0.8}$(O)OH exhibits more excellent electronic structure characteristics and strong spin polarization behaviour compared with NiFe(O)OH, NiFeMn(O)OH and NiFeCe$_{0.8}$(O)OH. In NiFe(O)OH, the d-band center is located at −1.511 eV, significantly below the Fermi level, which is unfavourable for effective adsorption of reaction intermediates (Fig. 5d). The incorporation of Ce shifts the d-band center closer to the Fermi level through hybridization between Ce 4f and Ni/Fe 3d orbitals, thereby enhancing the adsorption strength of O and OH intermediates. Mn doping further modulates the d-orbital energy distribution *via* its unpaired 3d electrons, bringing the d-band center closer to the optimal range for adsorption. NiFeMnCe$_{0.8}$(O)OH also exhibits a higher density of d states and a narrower band gap near the Fermi level, indicating enhanced electrical conductivity and electron mobility. This optimized electronic structure enables efficient use of spin-polarized electrons at key energy levels and enhances their response to external magnetic fields, leading to a pronounced magnetic enhancement.

Free energy calculations reveal that NiFeMnCe$_{0.8}$(O)OH exhibits enhanced control over reaction intermediates. At $U = 0$ V, the potential-determining step (PDS) for NiFe(O)OH, NiFeMn(O)OH, and NiFeCe$_{0.8}$(O)OH is the conversion of *O to *OOH, indicating that *OOH formation is the main thermodynamic barrier (Fig. 5e). In contrast, for the NiFeCe$_{0.8}$(O)OH, the PDS shifts to *OOH desorption (*OOH → O_2) with the lowest energy barrier, suggesting weakened *OOH binding and improved oxygen release. This is attributed to the synergistic effect of Ce and Mn: Ce promotes oxygen vacancy formation and reduces *OOH binding through its redox activity, while Mn adjusts the Fe electronic state to further optimize *OOH adsorption. At the standard potential ($U = 1.23$ V), the PDS for NiFe(O)OH, NiFeMn(O)OH, and NiFeCe$_{0.8}$(O)OH remains at *OOH formation (Fig. 5f). However, for NiFeMnCe$_{0.8}$(O)OH, it shifts to *OH adsorption, indicating a change in the reaction pathway at high potentials. This shift likely arises from the redistribution of the electronic structure under anodic bias,

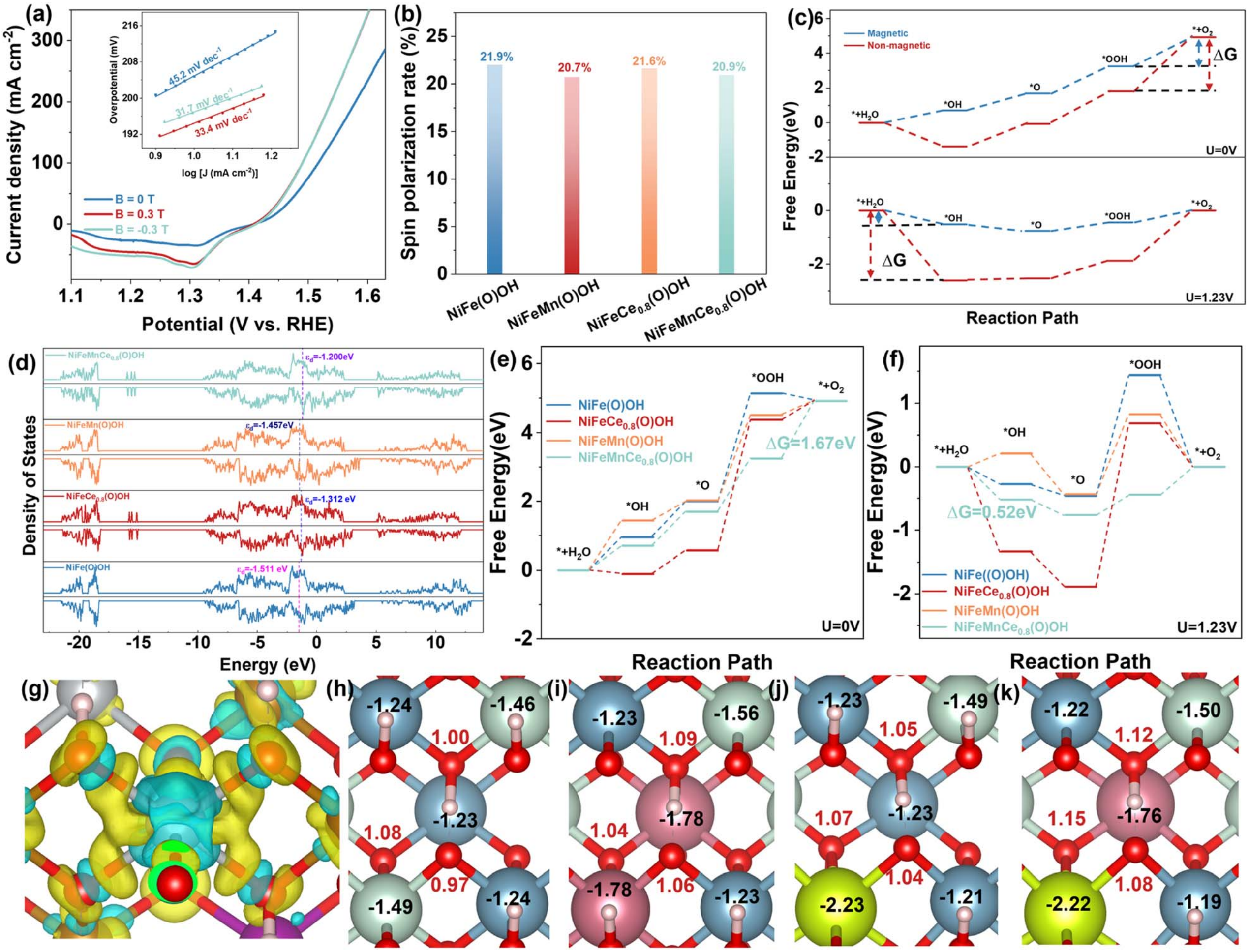

Fig. 5 (a) Comparison of LSV curves at $B = 0$ and ± 0.3 T without iR-compensation (inset: Tafel slopes). (b) Spin polarization ratios of different catalysts. (c) Gibbs free energy diagrams of NiFeMnCe$_{0.8}$(O)OH with and without spin polarization. (d) TDOS Gibbs free energy diagram on NiFeMnCe$_{0.8}$(O)OH at (e) $U = 0$ V and (f) $U = 1.23$ V. (g) The charge density difference on Ni site in NiFeMnCe$_{0.8}$(O)OH. The Bader charge in (h) NiFe(O)OH, (i) NiFeMn(O)OH, (j) NiFeCe$_{0.8}$(O)OH and (k) NiFeMnCe$_{0.8}$(O)OH.

which reduces the affinity of Ni sites for nucleophilic OH$^-$ species, thereby increasing the free energy barrier of this step.

The multi-metal synergistic effect on the electronic structure evolution during OER in NiFeMnCe$_{0.8}$(O)OH is investigated through differential charge density and Bader charge analyses. Fig. 5g displays the charge distribution around Fe, Ce, Mn, and Ni sites, with yellow and cyan isosurfaces representing electron accumulation and depletion, respectively. Fe and Ce show moderate charge redistribution, indicating their roles in charge regulation and transfer. Mn and Ni exhibit stronger charge polarization, especially electron accumulation around Ni, highlighting its key role as an electron exchange center in OER.

Bader charge analysis quantifies charge transfer in each system. In NiFe(O)OH, Ni and Fe lose limited electrons, leading to minimal overall charge rearrangement (Fig. 5h). Upon Mn doping, Mn undergoes substantial electron loss ($-1.78|e|$) (Fig. 5i), which enhances the electron density of Ni, thereby improving its electronic environment. In NiFeCe$_{0.8}$(O)OH, Ce experiences significant electron depletion ($-2.23|e|$) and modulates the electronic states of neighboring metals (Fig. 5j), reflecting its effective charge buffering and coupling effect. In NiFeMnCe$_{0.8}$(O)OH, Mn and Ce continuously donate electrons, stabilizing electron transfer pathways, while the Ni site maintains a high electron density ($-1.22|e|$) (Fig. 5k). Enhanced electron accumulation around adjacent oxygen atoms further strengthens Ni's role as the active center for OER. In summary, Fe maintains structural stability, while Mn and Ce significantly enhance the electronic state and reactivity of Ni active sites through strong electron supply and charge rearrangement, creating a microscopic environment conducive to intermediate adsorption and electron transport.

Conclusions

In this study, medium-entropy Ni–Fe–Mn–Ce oxyhydroxide catalysts have been successfully constructed by *in situ* reconstruction. The NiFeMnCe$_{0.8}$(O)OH exhibits excellent oxygen evolution performance in both 1 M KOH and alkaline seawater, achieving low overpotentials of 183 mV and 224 mV at 10 mA cm^{-2}, respectively. It maintains stability at high current (1 A cm^{-2}) while suppressing chlorine evolution. *Operando* characterization combined with DFT calculations reveal that the multivalent nature of Ce enables precise modulation of the transition metal d-band center position, thereby optimizing metal–oxygen bond strength. Meanwhile, Mn incorporation alters orbital energy level distribution to enhance the adsorption–desorption capacity of key reaction intermediates. The synergistic spin polarization effects between these elements not only significantly accelerate interfacial charge transfer kinetics but also reconfigure the OER pathway by reducing the adsorption energies of key intermediates (*OOH, *O). This dual modulation mechanism collectively lowers the reaction energy barriers, accounting for the observed enhancement in catalytic activity and selectivity under alkaline seawater conditions. This work advances both seawater electrolysis catalyst design and medium-entropy material applications in electrochemical energy systems.

Author contributions

Liyuan Xiao: writing – original draft, investigation, data curation. Xue Bai: investigation. Zhenlu Wang: investigation. Jingqi Guan: writing – review & editing, supervision, project administration, conceptualization.

Conflicts of interest

There are no conflicts to declare.

Data availability

The data supporting this article have been included as part of the supplementary information (SI). Supplementary information: synthetic methods, material characterization, electrochemical measurements, theoretical calculation details, supplementary diagrams (SEM, EDX, Raman, LSV, CV, XPS, *etc.*) and supplementary tables. See DOI: https://doi.org/10.1039/d5sc05118e.

Acknowledgements

This work was supported by the National Natural Science Foundation of China (No. 22075099).

References

1 Q. Qian, Y. Zhu, N. Ahmad, Y. Feng, H. Zhang, M. Cheng, H. Liu, C. Xiao, G. Zhang and Y. Xie, *Adv. Mater.*, 2024, **36**, 2306108.
2 I. Slobodkin, E. Davydova, M. Sananis, A. Breytus and A. Rothschild, *Nat. Mater.*, 2024, **23**, 398–405.
3 M. Chen and J. Guan, *Adv. Funct. Mater.*, 2025, 2423552.
4 J. Han, J. Sun, S. Chen, S. Zhang, L. Qi, A. Husile and J. Guan, *Adv. Mater.*, 2024, **36**, 2408139.
5 X. Xu and J. Guan, *Chem. Sci.*, 2024, **15**, 14585–14607.
6 L. Xiao, X. Bai, J. Han, T. Tang, S. Chen, H. Qi, C. Hou, F. Bai, Z. Wang and J. Guan, *Nano Res.*, 2024, **17**, 2429–2437.
7 B. Wang, J. Chen, L. Luo, G. Huang, Q. Shi, Q. Wei, M. Shang and Q. Liu, *Adv. Funct. Mater.*, 2025, 2505763.
8 Q. Li, W. Luo, X. Cui and J. Shi, *Angew. Chem., Int. Ed.*, 2025, **64**, e202500303.
9 S. Bai, W. Dai, X. Chen, F. Zhang, W. Chen, B. Wu, C. Zhao, J. Guo and S. Huang, *Nano Res.*, 2025, **18**, 94907809.
10 B. Wu, W. Dai, X. Yang, C. Zhao, Y. Zhang, C. Cui, Y. Sui, P. Cao and S. Huang, *Fuel*, 2024, **374**, 132450.
11 X. Zou, M. Tang, Q. Lu, K. Zhang, L. Wu, Z. Shao and L. An, *Adv. Energy Mater.*, 2025, 2501496.
12 L. Lei, D. Huang, C. Zhou, S. Chen, X. Yan, Z. Li and W. Wang, *Coord. Chem. Rev.*, 2020, **408**, 213177.
13 Y. Zhu, J. Wang, G. Weiser, M. Klingenhof, T. Koketsu, S. Liu, Y. Pi, G. Henkelman, X. Shi, J. Li, C.-W. Pao, M.-H. Yeh, W.-H. Huang, P. Strasser and J. Ma, *Adv. Energy Mater.*, 2025, 2500554.
14 D. Chanda, H. Kwon, M. M. Meshesha, J. S. Gwon, M. Ju, K. Kim and B. L. Yang, *Appl. Catal., B*, 2024, **340**, 123187.
15 D. Zhang, H. Li, H. Lu, Z. Yin, Z. Fusco, A. Riaz, K. Reuter, K. Catchpole and S. Karuturi, *Energy Environ. Sci.*, 2023, **16**, 5065–5075.
16 F. Zhu, Z. Du, K. Xu, F. He, Y. Xu, Y. Liao and Y. Chen, *Adv. Energy Mater.*, 2024, **14**, 2401048.
17 H. Wu, Z. Li, Z. Wang, Y. Ma, S. Huang, F. Ding, F. Li, Q. Zhai, Y. Ren, X. Zheng, Y. Yang, S. Tang, Y. Deng and X. Meng, *Appl. Catal., B*, 2023, **325**, 122356.
18 W. Cao, X. Yang, W. Dai, B. Wu, Y. Zhang, C. Zhao, Y. Sui and S. Huang, *New J. Chem.*, 2023, **47**, 12670–12677.
19 L. Zhu, M. Wang, S. Xiang, D. Sun, Y. Tang and H. Wang, *Adv. Energy Mater.*, 2023, **13**, 2302046.
20 S. Bai, W. Dai, X. Yang, B. Wu, J. Guo, C. Zhao, Y. Zhang, C. Cui, G. Zou and S. Huang, *Int. J. Hydrogen Energy*, 2024, **84**, 615–622.
21 W. Dai, X. Yang, F. Hu, W. Cao, C. Zhao, Y. Zhang and S. Huang, *J. Alloys Compd.*, 2023, **952**, 169987.
22 R. Yan, H. Yin, X. Zuo, W. Peng, X. Zhu, L. Shi, J. Hou, D. Wang, F. Ye, J. Li, B. Mao and C. Hu, *Appl. Catal., B*, 2025, **361**, 124609.
23 M. Chen, N. Kitiphatpiboon, C. Feng, A. Abudula, Y. Ma and G. Guan, *eScience*, 2023, **3**, 100111.
24 X. Liu, J. Chi, H. Mao and L. Wang, *Adv. Energy Mater.*, 2023, **13**, 2301438.
25 Y. Yu, W. Zhou, X. Zhou, J. Yuan, X. Zhang, X. Meng, F. Sun, J. Gao and G. Zhao, *Adv. Funct. Mater.*, 2025, **35**, 2419871.
26 H. Du, X. Wang, J. Song, N. Ran, J. Ma, J. Wang and J. Liu, *Adv. Funct. Mater.*, 2024, **34**, 2407586.
27 L. Xiao, X. Bai, J. Han, Z. Wang and J. Guan, *Chin. J. Catal.*, 2025, **71**, 340–352.
28 J. Han, C. Hou, S. Jiao, X. Niu, L. Li and J. Guan, *Nano Energy*, 2025, **140**, 111071.
29 L. Tan, H. Wang, C. Qi, X. Peng, X. Pan, X. Wu, Z. Wang, L. Ye, Q. Xiao, W. Luo, H. Gao, W. Hou, X. Li and T. Zhan, *Appl. Catal., B*, 2024, **342**, 123352.
30 L. Wang, K. Huang, X. Zheng, Y. Liu, J. Wu, Q. Dai, Z. Chen, Z. Li, B. Yang, C. Lian, L. Lei and Y. Hou, *Adv. Funct. Mater.*, 2025, 2417603.

31 Z.-F. Huang, S. Xi, J. Song, S. Dou, X. Li, Y. Du, C. Diao, Z. J. Xu and X. Wang, *Nat. Commun.*, 2021, **12**, 3992.

32 J. Mu, C. Yu, X. Song, L. Chen, J. Zhao and J. Qiu, *Adv. Funct. Mater.*, 2025, 2423965.

33 Y. Wang, Y. Zhuang, G. Yang, C. Dong and M. He, *Small*, 2024, **20**, 2404205.

34 F. Sun, G. Wang, Y. Ding, C. Wang, B. Yuan and Y. Lin, *Adv. Energy Mater.*, 2018, **8**, 1800584.

35 B. Yuan, C. Li, Y. Liu, C. Wang, L. Guan, K. Li and Y. Lin, *Int. J. Hydrogen Energy.*, 2019, **44**, 11705–11716.

36 K. Zhu, X. Zhu and W. Yang, *Angew. Chem., Int. Ed.*, 2019, **58**, 1252–1265.

37 Y. Wang, S. Li, X. Hou, T. Cui, Z. Zhuang, Y. Zhao, H. Wang, W. Wei, M. Xu, Q. Fu, C. Chen and D. Wang, *Adv. Mater.*, 2024, **36**, 2412598.

38 C. Hu, Y. Hu, C. Fan, L. Yang, Y. Zhang, H. Li and W. Xie, *Angew. Chem., Int. Ed.*, 2021, **60**, 19774–19778.

39 J.-O. Shim, H.-S. Na, A. Jha, W.-J. Jang, D.-W. Jeong, I. W. Nah, B.-H. Jeon and H.-S. Roh, *Chem. Eng. J.*, 2016, **306**, 908–915.

40 M. Shen, L. Lv, J. Wang, J. Zhu, Y. Huang and J. Wang, *Chem. Eng. J.*, 2014, **255**, 40–48.

41 R. Jain and S. Gulati, *Vib. Spectrosc.*, 2023, **126**, 103540.

42 K. H. Cho, S. Park, H. Seo, S. Choi, M. Y. Lee, C. Ko and K. T. Nam, *Angew. Chem., Int. Ed.*, 2021, **60**, 4673–4681.

43 X. He, X. Han, X. Zhou, J. Chen, J. Wang, Y. Chen, L. Yu, N. Zhang, J. Li, S. Wang and H. Jin, *Appl. Catal., B*, 2023, **331**, 122683.

44 Y. Zeng, Z. Cao, J. Liao, H. Liang, B. Wei, X. Xu, H. Xu, J. Zheng, W. Zhu, L. Cavallo and Z. Wang, *Appl. Catal., B*, 2021, **292**, 120160.

45 H. Xu, G. Xin, W. Hu, Z. Zhang, C. Si, J. Chen, L. Lu, Y. Peng and X. Li, *Appl. Catal., B*, 2023, **339**, 123157.

46 Z. Gong, J. Liu, M. Yan, H. Gong, G. Ye and H. Fei, *ACS Nano*, 2023, **17**, 18372–18381.

47 Y. Chen, Y. Liu, W. Zhai, H. Liu, T. Sakthivel, S. Guo and Z. Dai, *Adv. Energy Mater.*, 2024, **14**, 2400059.

48 C. Rong, X. Huang, H. Arandiyan, Z. Shao, Y. Wang and Y. Chen, *Adv. Mater.*, 2025, **37**, 2416362.

49 Y. a. Zhu, F. Wu, X. Zhang, Y. Lin, L. Zhang, T.-S. Chan, Q. Zhang and L. Chen, *Adv. Mater.*, 2025, **37**, 2500449.

50 X. Wang, H. Zhong, S. Xi, W. S. V. Lee and J. Xue, *Adv. Mater.*, 2022, **34**, 2107956.

51 L. Yu, J. Xiao, C. Huang, J. Zhou, M. Qiu, Y. Yu, Z. Ren, C. W. Chu and J. C. Yu, *Proc. Natl. Acad. Sci. U. S. A.*, 2022, **119**, e2202382119.

52 Z. Li, M. Liu, J. Yan and L. Y. S. Lee, *Chem. Eng. J.*, 2023, **473**, 145293.

53 Y. Tao, Z. Xu, R. Yan, Y. Sun and S. Lin, *J. Alloys Compd.*, 2025, **1010**, 177480.

54 Y. Xin, Q. Hua, C. Li, H. Zhu, L. Gao, X. Ren, P. Yang and A. Liu, *J. Mater. Chem. A*, 2024, **12**, 23147–23178.

55 Y. Huang, G. Xu, J. Peng, L. Yu, Y. Chu and X. Wang, *ACS Sustainable Chem. Eng.*, 2024, **12**, 11541–11549.

56 Q. Tu, W. Liu, M. Jiang, W. Wang, Q. Kang, P. Wang, W. Zhou and F. Zhou, *ACS Appl. Energy Mater.*, 2021, **4**, 4630–4637.

57 N. S. Sheikh, D. Leonori, G. Barker, J. D. Firth, K. R. Campos, A. J. H. M. Meijer, P. O'Brien and I. Coldham, *J. Am. Chem. Soc.*, 2012, **134**, 5300–5308.

58 J. Xu, C.-C. Kao, H. Shen, H. Liu, Y. Zheng and S.-Z. Qiao, *Angew. Chem., Int. Ed.*, 2025, **64**, e202420615.

59 Y. Zhu, Z. Cai, Q. Wei, R. Chen, F. Guo, Y. Jiang, Y. Xiao, J. Guo, Z. Wang, J. Zhong and N. Cheng, *Adv. Funct. Mater.*, 2025, 2503692.

60 X. Bo, Y. Li, X. Chen and C. Zhao, *Chem. Mater.*, 2020, **32**, 4303–4311.

61 J. Sun, S. Zhou, Z. Zhao, S. Qin, X. Meng, C.-H. Tung and L.-Z. Wu, *Energy Environ. Sci.*, 2025, **18**, 1952–1962.

62 H. Wan, M.-Y. Xie, B. Li, J.-H. Nie, T. Huang, L. Li, J.-H. Shi, M.-H. Xian, J.-R. Huang, W. Hu, G.-F. Huang, F. Gao and W.-Q. Huang, *J. Mater. Sci. Technol.*, 2025, **207**, 1–9.

63 L. Wu, X. Shen, Z. Ji, J. Yuan, S. Yang, G. Zhu, L. Chen, L. Kong and H. Zhou, *Adv. Funct. Mater.*, 2023, **33**, 2208170.

64 L. J. Titheridge, C. Wu, S. K. Sharma, C. Tiffin, D. Holland, Y. Mao, Z. Wang, G. I. N. Waterhouse, J. Li and A. T. Marshall, *Chem. Eng. J.*, 2025, **513**, 162322.

65 W. Zhang, Q. lv, L. Hou, J. Wang, Z. Long, X. Lu, X. Yu and X. Li, *J. Mater. Sci. Technol.*, 2025, **211**, 11–21.

66 X. Guo, X. Zheng, X. Hu, Q. Zhao, L. Li, P. Yu, C. Jing, Y. Zhang, G. Huang, B. Jiang, C. Xu and F. Pan, *Nano Energy*, 2021, **84**, 105932.

67 S. Chen, Z. Zheng, Q. Li, H. Wan, G. Chen, N. Zhang, X. Liu and R. Ma, *J. Mater. Chem. A*, 2023, **11**, 1944–1953.

68 Y. Yao, S. Sun, H. Zhang, Z. Li, C. Yang, Z. Cai, X. He, K. Dong, Y. Luo, Y. Wang, Y. Ren, Q. Liu, D. Zheng, W. Zhuang, B. Tang, X. Sun and W. Hu, *J. Energy Chem.*, 2024, **91**, 306–312.